The Planetary Science Journal, 6:53 (15pp), 2025 March https://doi.org/10.3847/PSJ/ad864d

Beyond Point Masses. IV. Trans-Neptunian Object Altjira Is Likely a Hierarchical Triple Discovered through Non-Keplerian Motion

Maia A Nelsen[1], Darin Ragozzine[1], Benjamin C. N. Proudfoot[1,2], William G. Giforos[1], and Will Grundy[3]
[1] Brigham Young University, Department of Physics and Astronomy, N283 ESC, Provo, UT 84602, USA
[2] Florida Space Institute, University of Central Florida, 12354 Research Parkway, Orlando, FL 32826, USA
[3] Lowell Observatory, Flagstaff, AZ 86001, USA
Received 2023 December 16; revised 2024 September 23; accepted 2024 October 9; published 2025 March 4

Abstract

Dynamically studying trans-Neptunian object (TNO) binaries allows us to measure masses and orbits. Most of the known objects appear to have only two components, except (47171) Lempo, which is the single known hierarchical triple system with three similar-mass components. Though hundreds of TNOs have been imaged with high-resolution telescopes, no other hierarchical triples (or trinaries) have been found among solar system small bodies, even though they are predicted in planetesimal formation models such as gravitational collapse after the streaming instability. By going beyond the point-mass assumption and modeling TNO orbits as non-Keplerian, we open a new window into the shapes and spins of the components, including the possible presence of unresolved "inner" binaries. Here we present evidence for a new hierarchical triple, (148780) Altjira (2001 UQ_{18}), based on non-Keplerian dynamical modeling of the two observed components. We incorporate two recent Hubble Space Telescope observations, leading to a 17 yr observational baseline. We present a new open-source Bayesian point-spread function fitting code called `nPSF` that provides precise relative astrometry and uncertainties for single images. Our non-Keplerian analysis measures a statistically significant ($\sim 2.5\sigma$) nonspherical shape for Altjira. The measured J_2 is best explained as an unresolved inner binary, and an example hierarchical triple model gives the best fit to the observed astrometry. Using an updated non-Keplerian ephemeris (which is significantly different from the Keplerian predictions), we show that the predicted mutual event season for Altjira has already begun, with several excellent opportunities for observations through $\sim$2030.

Unified Astronomy Thesaurus concepts: Trans-Neptunian objects (1705); Occultation (1148); Orbital motion (1179)

Materials only available in the online version of record: machine-readable table

1. Introduction

Some of the best observational constraints on the streaming instability (SI) hypothesis of planetesimal formation come from the orbital properties of trans-Neptunian object (TNO) binaries. In particular, models of post-SI gravitational collapse are able to match many properties of TNO binary orbits like the orientation and the wide separations with near-equal mass ratios (e.g., D. Nesvorný et al. 2019). These binaries are prevalent (W. M. Grundy et al. 2019) in the "cold classical" portion of the Kuiper Belt, where heliocentric inclinations are very low (especially when measured in dynamically meaningful terms of proper/free inclinations relative to the local forcing plane; see Y. Huang et al. 2022). The cold classical population is also thought to have formed in situ, and NASA's New Horizons mission observations of cold classical Arrokoth point to a specific example of SI formation (e.g., W. B. McKinnon et al. 2020).

Dynamically, much of the post-SI gravitational collapse process is about the evolution and flow of angular momentum. The shrinking cloud soon has an excess of angular momentum (per unit mass), which naturally forms wide near-equal-mass binaries. However, some of this angular momentum cascades down to the components of these binaries, which provides the initial conditions for the spins and shapes of the components. Most gravitational collapse models use effective particle sizes and other approximations that make it challenging to resolve the angular momenta of the individual components (D. Nesvorný et al. 2010, 2021; J. E. Robinson et al. 2020). Recent work by B. Polak & H. Klahr (2023) shows that collapsing pebble clouds in the outer solar system frequently form into many components, many of which are near-equal binaries in close or contact configurations. Future generations of models will hopefully consider the evolution of these systems beyond initial formation to determine how angular momentum is partitioned into the reservoirs of a wide binary and two spins, as this is an important observational constraint for future models.

Some formation models already show that the components of the main binary can have so much angular momentum that one or both of the individual components should itself be a binary (D. Nesvorný et al. 2010, 2021; J. E. Robinson et al. 2020). We would then distinguish between the "outer" binary and an inner binary (or binaries). The "hierarchical triple" or "hierarchical quadruple" configuration is a relatively dynamically stable endpoint even for near-equal-size components, as seen in stellar multiple systems. Presently, there is only one observational example of a hierarchical triple (sometimes called "trinary") configuration in the solar system: the TNO (47171) Lempo.

Whether caused by a nonspherical shape or an unresolved inner binary, non-Keplerian effects on the outer binary are a

sensitive probe of the angular momentum distribution *within* TNO binary systems (D. Ragozzine et al. 2024, hereafter Paper I). Such effects are also currently detectable for several TNO binaries (B. C. N. Proudfoot et al. 2024b, hereafter Paper II). We thus propose that the strength of non-Keplerian effects can be a probe and constraint on the next generation of SI and gravitational collapse models by providing information on the shapes and spins of TNO binary components. In this work, we go beyond point-mass models for the TNO (148780) Altjira (2001 UQ_{18}) to show that it is best explained as an unresolved hierarchical triple.

In 2023, the Hubble Space Telescope (HST) observed Altjira to get two more precise astrometric measurements as part of Program 17206 (PI: Proudfoot). We combine these observations, a new Keck observation, and previously published observations as described in Section 3. For the new HST data, we measure the mutual astrometry and photometry of these objects using a new open-source fitting program called `nPSF`,[4] which is described in Section 4. We then use the non-Keplerian astrometric orbit fitter `MultiMoon` (Paper I) to fit the new Altjira data in Section 5. In addition to the usual Keplerian model, we use a binary quadrupole–point-mass model and a hierarchical triple model to describe the observations. We find that a close hierarchical triple is the preferred model for Altjira in Section 6. We provide an ephemeris for Altjira to support the ongoing mutual event season, including quantifying the importance of using a non-Keplerian model, in Section 7. We interpret our results in Section 8 and conclude in Section 9.

2. Background

2.1. Hierarchical Triples in the Solar System

Systems of three gravitationally interactive bodies with similar masses (sometimes called "trinaries") are only long-term stable in a "hierarchical" configuration where the third object orbits in an "outer" orbit that is at least several times larger than the "inner" binary. (The other stable configuration of three bodies requires one object to be much more massive than the others, e.g., Haumea and its two moons.) Among planets and small bodies, the only well-characterized example of a hierarchical triple is the TNO (47171) Lempo. Since we will propose that Altjira is also a hierarchical triple, we discuss Lempo in more detail here.

Originally thought to be a binary, Lempo was barely resolved as a triple by the highest-resolution HST camera by S. D. Benecchi et al. (2010). A non-Keplerian three-point-mass model for the system shows an inner binary of the two larger (∼250 km diameter) objects separated by ∼850 km orbited by a smaller component (∼125 km) with a semimajor axis of ∼7600 km (Paper I). This configuration has about as much angular momentum in the inner binary as in the outer binary. However, something may be missing in our understanding of the Lempo system, since A. C. M. Correia (2018) find that it is dynamically unstable on timescales orders of magnitude shorter than the age of the solar system. One hypothesis for this inconsistency was that the existing approximate orbital model overestimated the eccentricities, but Paper I shows that a three-point-mass fit to the data preserves the significant eccentricities (∼0.12 for the inner binary, ∼0.29 for the outer binary). Paper I suggests that further work is needed to characterize and explain the Lempo system and its long-term evolution.

Despite being a relatively massive system, Lempo was barely resolved (0.″03 or about 1 pixel) with the HST's now-defunct Advanced Camera for Surveys (ACS) High Resolution Channel. Combined with the theoretical expectation for such objects, it seems likely that there are many more hierarchical triples (or quadrupoles) beyond the HST resolution limit, which is dozens of primary radii for typical TNOs. We note that there are a few recent HST surveys (Programs 14616 and 15821; PI: Porter) with no published results yet. When the tighter binaries are very close together (up to touching "contact hierarchical triples"), they may be detectable by measuring the unique lightcurve of contact or very close binaries (e.g., M. R. Showalter et al. 2021) or multichord stellar occultations (e.g., R. Leiva et al. 2020). But beyond quite small separations, such methods are also unable to detect inner binaries. For these reasons, Paper I suggests using non-Keplerian dynamical effects to detect and characterize such objects like we attempt in this work with Altjira.

2.2. Discussion of Previous Analyses of Altjira

The formation and properties of TNO binaries formed by SI may be different for different populations, so it is helpful to consider the heliocentric dynamical classification of Altjira. While it is a nonresonant classical object, its orbit is in the region where the cold and hot classical populations overlap. Specifically, Altjira's heliocentric orbital inclination is near the commonly used border between the cold and hot classical population, with a free/proper inclination of 5.°4 (Y. Huang et al. 2022). Depending on the cold/hot cutoff inclination, Altjira has sometimes been classified as part of either population in previous studies that sometimes used approximate classification methods. While free inclination suggests that Altjira is outside the core of the cold classical region, we can follow W. M. Grundy et al. (2012) to use the inclination distribution for these populations to make a probabilistic estimate of Altjira's membership in the cold-versus-hot classical population. Previous studies of inclination distributions often used the "sin i times Gaussian" model, but this (as well as the more commonly used Rayleigh distribution) is better thought of as an approximation to the von Mises–Fisher distribution best used for directional statistics like inclination values (e.g., I. C. Matheson et al. 2023). Using the updated mixture model of R. Malhotra & S. Roy (2023) for the free inclination distribution of observed nonresonant classical TNOs, we find that ∼7% of TNOs with free inclinations of Altjira are consistent with cold classicals. This is smaller compared to previous estimates because the cold classicals are tighter in free inclinations (and not because of the particular use of the directional statistics model). This probability is enhanced by the fact that the wide binary nature is a better match for the cold classical population. On the other hand, even though Altjira is a relatively wide binary (semimajor axis of 2% of its Hill radius), it would have had a reasonable chance of surviving dynamical implantation (D. Nesvorný & D. Vokrouhlický 2019) and perturbations by passing TNOs (e.g., H. M. Campbell et al. 2023), so its possible origin as a hot classical cannot be easily ruled out. As a final consideration, Altjira's color is more consistent with that of cold classicals. Altogether, we think it is quite reasonable in future studies to classify Altjira as a cold classical with a relatively high inclination. A planned

[4] Located at https://github.com/dragozzine/nPSF.

observation with JWST will provide powerful insight into Altjira's origin as well.

The second component of Altjira—the unnamed S/2007 (148780) 1—is only slightly fainter, on average; thus, this system appears to be a near-equal-mass binary. The Keplerian orbit was determined by W. M. Grundy et al. (2011) to have a period of about 139.5 days, a semimajor axis of about 9904 km, and a system mass of about 3.95×10^{18} kg. The orbit was eccentric and inclined by about 35° to the equatorial plane (W. M. Grundy et al. 2011). The overall system absolute magnitude is $H \simeq 6$. An approximate thermal measurement leads to estimated diameters of 246^{+38}_{-139} km and 221^{+31}_{-125} km for the two components (E. Vilenius et al. 2014). This is based on a weak detection and/or upper limits and involves the assumption of equal-albedo, equal-density spheres, so there is significant statistical and systematic uncertainty. These sizes correspond to a density of $0.30^{+0.50}_{-0.14}$ g cm^{-3} and albedo of $0.04^{+0.18}_{-0.01}$.

S. S. Sheppard (2007) obtained some sparse information on the lightcurve for Altjira and found some discernible variations over two nights of observations at the ∼0.1 mag level and concluded that more data were needed. W. M. Grundy et al. (2011) report that the secondary ranges from being 0.3 mag brighter to 0.6 fainter than the primary in five epochs spanning a year (and we confirm significant variability below). We thus expect that one or both components are highly elongated. Long-term non-Keplerian monitoring and/or resolved photometry can better determine how each of the components contributes to the angular momentum budget, but for our present modeling effort, we assume that only the primary is a nonspherical quadrupole while the secondary is assumed to be a point mass (see Paper I and further discussion below).

W. M. Grundy et al. (2011) find that Altjira is predicted to have mutual events—where the primary and secondary shadow and/or occult one another—around 2028. We confirm and update this prediction below. Although the observation of such mutual events is challenging and the interpretation even more so (e.g., D. L. Rabinowitz et al. 2020), it provides an exciting opportunity to probe the properties of the components of Altjira without having to wait for a stellar occultation.

2.3. Bayesian Parameter Inference

Below, we use Bayesian parameter inference to both measure new relative positions of Altjira and to infer orbit and spin parameters when combined with previous astrometry. Both modeling efforts use Bayesian parameter inference "fitting" methods to determine information about model parameters based on the data. For clarity, we describe here the basic properties of Bayesian parameter inference as applied to our modeling methods (see Papers I and II for more detailed discussion). Many of these techniques are standard statistical methods that can be explored further in other references (e.g., D. W. Hogg et al. 2010; D. Foreman-Mackey et al. 2013; D. W. Hogg & D. Foreman-Mackey 2018; A. Gelman et al. 2020; R. van de Schoot et al. 2021).

Bayesian parameter inference is philosophically based in the idea that our belief about parameters in a model is best described as probability distributions. When new data are added to a problem, the original probability distribution for a parameter (the "prior") is updated to a new probability distribution (the "posterior"). When using a single model, this update is controlled by a simplified version of the Bayes theorem where the posterior is the prior multiplied by the "likelihood," which is the probability that the observations would be obtained assuming the parameters are known. The prior is usually chosen to be "uninformative" within physically allowed limits (e.g., the masses must be positive) so that the data-driven likelihood is the primary determinant of the posterior. Parameter values that give high probability to the data (high likelihoods) are favored and thus have high posterior probability. Determining the likelihood requires a "noise model," and we use the common assumptions that the data (whether pixels or astrometry) are independent, each with a previously known uncertainty that is assumed to be Gaussian. Thus, our model for the likelihood is equivalent to the standard calculation of χ^2. It is thus likely that our Bayesian inference methods would give quite similar values for the "best fit" (or "maximum likelihood") compared to standard χ^2 minimization modeling. However, Bayesian inference is generally more accurate at estimating uncertainties, especially when these are correlated, because the posterior is a joint probability distribution over all parameters and thus can include correlations, degeneracies, etc. The main challenge with Bayesian methods is that they can be computationally expensive.

In realistic use cases, the posterior is determined numerically through an algorithm that returns a large list of sets of parameters ("posterior draws") that are samples from the posterior probability distribution. These posterior draws can then be studied, summarized, and simplified for presentation. The posterior probability distribution of a parameter is easily calculated by taking a histogram of the list of posterior draws. For example, a summary of the "best fit and uncertainties" for a single parameter is often determined by taking the posterior draws and finding the 50th percentile (e.g., the median) and using the 16th and 84th percentiles for the uncertainties (as we do below). When the posterior probability distribution is Gaussian (as is often the case), this is effectively equivalent to the typical understanding of best fit and uncertainties. As another example, the probability distribution of any calculation based on the inferred parameters can be determined by performing the calculation for each individual posterior draw and summarizing as before. For example, our model below infers parameters about the position of the objects in the image but then calculates the derived parameter of the relative astrometry, which is summarized as a best fit and uncertainty.

The most common algorithm for sampling from the posterior and generating the list of posterior draws is a Monte Carlo technique called Markov Chain Monte Carlo (MCMC). Starting with an initial guess, MCMC methods produce the desired list of posterior draws given a "forward model" that can evaluate the posterior probability (likelihood times prior) given a specified set of parameters. Like all optimization methods, MCMC requires an initial guess that strongly affects the first iterations, and this "burn-in" or "warm-up" portion of the algorithm should be removed. The size of the burn-in is determined by visual inspection of the outputs (though it is often specified in advance for convenience). Our algorithms include a step after the prespecified burn-in that removes severely underperforming walkers and replaces them with combinations of remaining walkers and then runs a short additional burn-in (see Paper I).

Different MCMC algorithms proceed differently from the initial guess with varying levels of efficiency and complexity. In every case, the algorithm proposes a new "link" in the

"chain" based on the current set of parameters. This new link is either accepted (because it has a better posterior probability, though lower-probability links are accepted probabilistically to properly explore the parameter space) or the current link is repeated. Another analogy for this process, which we use, is that of a "walker" taking "steps" around the parameter space.

Parallel processing and statistical advancements have led to the very highly used *emcee* algorithm for MCMC sampling (D. Foreman-Mackey et al. 2013). This algorithm uses an ensemble of walkers (or chains) and the property of the ensemble to automatically learn about the shape of the parameter space (e.g., parameter scales and correlations). This is a very effective method for sampling from posteriors with moderate numbers of parameters that do not have widely separated modes (e.g., local minima or disconnected regions of parameter space that are good fits). Both of our fitting algorithms reasonably satisfy these criteria.

Like all Monte Carlo methods, continued sampling (slowly) increases the accuracy of the sampling algorithm in representing the true posterior distribution. We choose to take a sufficiently large number of samples (after discarding the burn-in) so that the uncertainties in our parameters are characterized well enough that our scientific conclusions are relatively robust.

By exploiting Bayesian parameter inference through *emcee*, we are able to fit models to our data using state-of-the-art statistical and computational methods.

3. Observations

Non-Keplerian effects evolve on much slower timescales than the binary orbital period, so we benefit significantly in extending the baseline of observations with new data from HST and Keck. These observations for determining Altjira's binary orbit focus on the precise relative astrometric positions needed for orbit fitting. We use the original eight data points from W. M. Grundy et al. (2011) as they are. These come from HST/ACS, HST/WFPC2, and Keck, as discussed in W. M. Grundy et al. (2011). We combine these with an additional observation obtained from Keck and two new observations from HST/WFC3.

Keck observations of the system were obtained on 2020 January 5 at a mean time of 9:06 UTC and mean air mass of 1.34. We used the NIRC2 narrow-field infrared camera with a plate scale of 100.5 pixels arcsec^{-1} along with the Keck II laser guide star adaptive optics system (D. Le Mignant et al. 2006) to correct for the smearing effect of atmospheric turbulence. A nearby 13th magnitude star was used for tip–tilt correction. A total of six usable 180 s exposures were recorded through the H filter, with exposure pairs recorded in each of three consecutive dither positions. After flat-fielding and subtracting the other dither positions, astrometry was done on each of the coadded pairs by fitting a Lorentzian point-spread function (PSF) with the same width parameters to each of the two components in the image. Plate scale and camera orientation details were taken from S. Yelda et al. (2010). Based on prior experience with this instrument configuration with targets of similar faintness, the 1σ astrometric uncertainties were taken as 3 mas, although the scatter between the measurements from the three dither positions was somewhat smaller than that.

As part of HST Program 17206, two additional single-orbit visits of Altjira were acquired in 2023. These visits each consisted of six dithered observations using HST's WFC3 scheduled at times at which our preliminary analysis indicated that the positions of the two system components had the most uncertainty in previous modeling (i.e., high "information gain," as discussed in Paper II). These two visits were designed to achieve high astrometric precision by maximizing signal-to-noise with observations using HST's wide F350LP filter.

4. Fitting an Arbitrary Number of PSFs with `nPSF`

We here introduce a new open-source[5] precise PSF fitting routine called `nPSF`. `nPSF` works similarly to the description of PSF fitting routines in W. M. Grundy et al. (2008) and D. Ragozzine & M. E. Brown (2009), which are standard in the field. We then use `nPSF` to measure astrometry for the two observations from HST/WFC3. These methods are enhanced by the use of Bayesian parameter inference methods discussed above.

4.1. How `nPSF` Works

For solar system small bodies, it is common that the separation of the sources is several pixels and the width of the PSF (e.g., the FWHM) is only a few pixels. Even when the separation is comparable to the FWHM, it is possible to perform relative astrometry until the separation is less than $\sim$2 pixels, where it becomes very challenging, if not impossible, even for equally bright sources (e.g., S. D. Benecchi et al. 2010). Even when the separation is clearly larger than the FWHM (the components are "resolved"), the light from the sources may overlap, requiring simultaneous modeling of each of the sources.

Precise relative astrometry depends on accurately measuring the center of light of two or more sources. HST benefits from having a very stable and well-understood PSF as a function of camera, filter, approximate pixel location, and telescope focus value. We use theoretical supersampled PSFs as provided by the well-known TinyTim software package (J. E. Krist et al. 2011) with occasional approximations (e.g., not using the exact pixel locations of the sources in the PSF generation process). Though TinyTim is not officially recommended for accurate WFC3 PSF modeling, we note that precise relative astrometry does not require highly accurate PSFs because measuring the center of light (basically the position-weighted average of the counts) is relatively robust relative to the statistical precision for these faint objects. We have tested this by using the "wrong" PSF model for synthetically generated data, which leads to an insignificant systematic effect.

`nPSF` models each image separately. A subsection of the image (e.g., 50 $\times$ 50 pixels) approximately centered on the primary component is selected. Cosmic rays are cleaned using the method of P. G. van Dokkum (2001) as implemented by C. McCully & M. Tewes (2019). The median of the pixels is subtracted to remove any overall constant background. Pixel-by-pixel uncertainties are accounted for using a Poisson photon noise model. This allows us to gather uncertainties from each image individually that are fully propagated to astrometric uncertainties.

Using standard methods, a model image is constructed for comparison to the observations. At the beginning of the analysis, the user can choose n, the number of PSFs to include in the model. The model requires multiple free parameters, primarily the x- and y-positions and "heights" (e.g., the total

[5] https://github.com/dragozzine/nPSF

Table 1
Derived Astrometry from HST Images Taken in 2023 February and October

Time	Δ Lat.	Δ Long.	Δ Lat. Error	Δ Long. Error
2459982.70877	−0.067317	0.157316	0.00091621	0.00080187
2459982.71397	−0.066984	0.159926	0.00082586	0.00076244
2459982.71927	−0.067997	0.158797	0.00090732	0.00081523
2459982.72456	−0.065999	0.158752	0.00092021	0.00082179
2459982.72976	−0.067761	0.158984	0.00088429	0.00079804
2459982.71927	−0.067212	0.158755	0.00089078	0.00079987
2460240.8251	0.083471	−0.169464	0.00110204	0.00102173
2460240.8303	0.084002	−0.170261	0.00110006	0.00102710
2460240.8406	0.082228	−0.171161	0.00113814	0.00108419
2460240.8457	0.083687	−0.170873	0.00110498	0.00108649
2460240.8509	0.081580	−0.171009	0.00115472	0.00109073
2460240.8418	0.0829938	−0.17055	0.00111999	0.00106205

Note. Table of derived astrometry from each new HST/WFC3 image from `nPSF` as well as the averages from each visit. Time is in "System" Julian Date, e.g., with the light-travel time correction to Altjira included. Relative positions are given in J2000 ecliptic coordinates.

brightness), for each PSF. We also allow the HST focus to be a free parameter by generating a grid of model PSFs with different focus values. The floating focus parameter is then rounded to the value of the nearest pregenerated PSF. With a fine enough grid of focus values, we closely approximate having a fully floating focus parameter. This approximately models HST "breathing" and also allows for some compensation for the fact that the theoretical model PSF is likely not an exact match to the observed PSF. The PSFs are inserted at their model locations using fractional pixel shifts of the supersampled theoretical PSFs. We include the charge diffusion kernel contained within each modeled TinyTim PSF. Using our noise model, we calculate the overall likelihood by summing the log likelihoods of each individual pixel; that is, we reasonably assume that all pixel counts are independent.

We use Bayesian parameter inference (discussed in detail above in Section 2.3) to explore the range of models (although an optimization mode is also implemented). This determines the "posterior" probability distribution, e.g., a list of self-consistent sets of parameters that are a good match to the data and that also automatically provide uncertainties and correlations between each parameter. We use the `emcee` package. Priors are generally uninformative, and initial guesses are set by visual inspection of the image. After fitting for image coordinates, the `pixel-to-world` function in `astropy` (The Astropy Collaboration et al. 2013) uses information in the image headers to calculate the posterior distribution of the relative astrometric offsets in R.A. and decl. Internally, `MultiMoon` uses time as measured from a clock located at the TNO and relative astrometry in ecliptic coordinates. A final step in `nPSF` outputs a single line of astrometric data in these units that can be copied directly into an observation file for `MultiMoon`.

After completing the prespecified number of MCMC sampling steps, `nPSF` generates plots to allow for visual inspection of the sampling as well as sample images for the parameters with the maximum likelihood. The time taken for a single likelihood evaluation is very short (tens of milliseconds), so `nPSF` is not explicitly parallelized. A typical run takes less than ∼1 day of wall clock time for a single CPU to analyze a single image, even for an extensive exploration of parameter space.

We performed a suite of injection and recovery tests to confirm that `nPSF` was working well and to test the limits of its performance. For example, under ideal injection and recovery conditions, we find that it can just successfully recover a secondary when the separation in pixels is about the same as the brightness difference in magnitudes. We have also validated `nPSF` on a variety of past HST programs, focusing on Trans-Neptunian Binary astrometry and finding adequate consistency with published observations.

We note that even though the processes are similar in theory, we found that PSF fitting problems can be very different in practice depending on where they fall along three axes: semiresolved versus well-resolved, similar brightnesses versus unequal brightnesses, and measurement of a known source versus detecting a new source (or placing upper limits). `nPSF` does well for known objects with similar brightnesses even with close separations. It is not automatically ideal for semiresolved unequal brightnesses without some extra care (e.g., setting a prior for the brightness ratio of the components). It can be used to provide approximate upper limits for nondetections, but injection/recovery tests would be more accurate and significant.

4.2. Application of `nPSF` to Altjira HST Images

We used `nPSF` on the two epochs (2023 February and October) of HST/WFC3 images of Altjira. All 12 images were run with initial guesses based on inspection of the image and all model parameters for a two-PSF fit. We used 2500 burn-in steps and 2500 additional steps for 100 walkers, except for one image from the October visit that needed 500 extra steps to sample well. One image from each visit was excluded due to systematic errors and problems with cosmic-ray masking, which did not allow their fits to converge. The other five images appeared converged based on visual inspection and had no issues. The derived astrometry and uncertainties are shown in Table 1.

The results for Altjira have the observed positions reasonably near the positions predicted based on previous data. They also have very small (submilliarcsecond) uncertainties. In February and October, the secondary was 0.21 and 0.57 mag fainter than the primary, respectively.

Table 2
Relative Astrometry for (148780) Altjira

Julian Date	Date	Telescope	Instrument/Camera	$\Delta\alpha\cos\delta$	$\Delta\delta$	$\sigma_{\Delta\alpha\cos\delta}$	$\sigma_{\Delta\delta}$
2453953.767	2006 Aug 6	HST	ACS-HRC	−0.17182	0.06302	0.00109	0.00408
2454306.58	2007 Jul 25	HST	WFPC2-PC	−0.16332	−0.03667	0.00167	0.00168
2454320.431	2007 Aug 8	HST	WFPC2-PC	−0.27679	−0.00742	0.00204	0.001
2454380.396	2007 Oct 6	HST	WFPC2-PC	−0.05278	0.04552	0.001	0.0019
2454416.885	2007 Nov 12	HST	WFPC2-PC	0.14054	−0.06317	0.00138	0.00118
2454672.799	2008 Jul 25	HST	WFPC2-PC	0.15723	−0.00858	0.00133	0.00143
2455176.892	2009 Dec 11	Keck II	NIRC2	−0.36534	0.03793	0.003	0.003
2455412.109	2010 Aug 3	Keck II	NIRC2	−0.03594	−0.03938	0.006	0.003
2458884.879	2020 Feb 5	Keck II	NIRC2	0.18001	−0.06656	0.003	0.003
2459982.981	2023 Feb 7	HST	WFC3	0.16501	−0.04991	0.00092	0.00079
2460241.099	2023 Oct 23	HST	WFC3	−0.17699	0.06817	0.00065	0.0011

Note. The relative R.A. ($\Delta\alpha\cos\delta$) and decl. ($\Delta\delta$) positions of Altjira's secondary, along with measurement uncertainties in arcseconds. Julian Date is geocentric; the specific location of the observatories is negligible and ignored.

nPSF uses pixel-by-pixel uncertainties that are used to determine confidence intervals for relative positions for each individual image. Current practice combines these into a single astrometric measurement by taking the mean and standard deviation of the best-fit positions from each image (after discarding obvious outliers). The rationale for this is that such a technique is better at incorporating systematic uncertainties, though using the standard deviation of the best fits is not an ideal way of propagating uncertainty, especially when only a few images are used. For these observations, the standard deviation of best-fit values is quite similar to the reported uncertainties. If the image-by-image uncertainties were accurate, the standard deviation of the positions would be about $\sqrt{5}$ times smaller; this suggests that there are systematic effects so that our image-by-image uncertainties are optimistic.

We explicitly tested the difference between using image-by-image uncertainties and the best-fit averaging method in our MultiMoon fits and found that the results were not significantly different in accuracy or precision of the important orbit and spin parameters. For consistency with previous modeling methods, and to account for systematic uncertainties, we use the average points and their standard deviations in our detailed analysis below.

Most of the time, the relative motion of the components of Altjira is less than 1 mas hr^{-1}. Thus, we do not expect to see, nor do we see, motion during the course of the observations. In other solar system small bodies, motion can be much faster, suggesting that image-by-image nPSF analysis would be more accurate in providing astrometry that includes information about the motion instead of averaging it out.

We discuss below the possibility that one or both of the components of Altjira may themselves be a close binary. We checked the residuals of the nPSF astrometry fits but found no clear evidence for a third object in the images. This is consistent with the expected separations of these binaries derived below, which are far below the resolution limit.

5. Methods

Combining all the relative astrometric measurements for Altjira provides the observational constraints on our orbit modeling. These are summarized in Table 2.

We fit these data using three different orbit models: a Keplerian (two-point-mass) model, a binary non-Keplerian model of a quadrupole and a point mass, and a non-Keplerian model of three point masses. To accommodate non-Keplerian orbital modeling, we use the MultiMoon code powered by the SPINNY *n*-quadrupole integrator. A detailed explanation and validation of SPINNY and MultiMoon is provided in Papers I and II, but we provide an overview of key aspects here before discussing our analysis for Altjira specifically.

5.1. The SPINNY n-quadrupole Model

SPINNY integrates the orbit and spin dynamics of an arbitrary number of quadrupoles or point masses (as in A. C. M. Correia 2018). Quadrupoles are characterized by a spherical harmonic expansion of the potential where J_2R^2 and $C_{22}R^2$ quantify the oblateness and prolateness, respectively. The orientation of the quadrupole is described using Euler angles equivalent to orbital elements such as the "spin inclination" $i_{\rm sp}$; these are defined relative to the J2000 ecliptic frame. For small bodies like the components of Altjira, the dominant contribution to the quadrupole strength is the shape and orientation of the body, not the interior mass distribution. However, these spherical harmonic terms do not uniquely provide information on the shape, so an assumed shape model is required to calculate a specific value of J_2. For example, assuming a triaxial ellipsoid model with semiaxes a, b, and c, J_2R^2 and $C_{22}R^2$ can be used to determine the overall shape by using the following equations:

$$a = \sqrt{5J_2R^2 + c^2 + 10C_{22}R^2}, \quad (1)$$

$$b = \sqrt{5J_2R^2 + c^2 - 10C_{22}R^2}, \quad (2)$$

as discussed in more detail in Papers I and II.

SPINNY calculates the spin–orbit coupling (including the back torque of the orbit on the spin of the body), which leads to both apsidal and nodal precession. In practice, there are many degeneracies between the model parameters and some parameters that are not constrained by the observations. For example, the spin rate, the prolateness ($C_{22}R^2$), and the angle associated with the long axis of the quadrupole ($\omega_{\rm sp}$) are practically unconstrained when the spin period is much shorter than the orbital period because the rotational effects easily average out. In the case of Altjira, short-term variability from S. S. Sheppard (2007) combined with the relatively wide separation of the binary means that these parameters are not expected to be meaningfully constrained, though we do include them in our model for completeness. Furthermore, we have

found that there can be many degeneracies when considering a model with two quadrupoles, even if only the oblateness terms are considered. Generally speaking, the observed non-Keplerian motion is mostly due to orbital precession, which is the sum of precessions caused by the two quadrupoles. (Technically, this assumes that most of the angular momentum is in the orbit, which is the case for Altjira; the case where there are three angular momenta reservoirs is poorly understood.) Similar to how a Keplerian model can only determine the sum of the masses, Altjira's observational data can only constrain a weighted sum of the J_2R^2 values for the two components. Based on theoretical expectations (see Papers I and II), we hypothesize that the approximate quantity measured is $M_1 J_{2,1} R_1^2 \cos\phi_1 + M_2 J_{2,2} R_2^2 \cos\phi_2$, where M_i is the mass of each object and ϕ_i is the obliquity of the spin to the orbit. This implies that the unknown mass partitioning between the two components affects the interpretation of the shapes; on the other hand, extensive observations and non-Keplerian modeling can break the mass degeneracy in certain cases.

Thus, for simplicity, we consider only the primary as having a nonspherical shape and thus call this the binary quadrupole–point-mass model. In actuality, the two components are similar brightnesses and thus presumably have similar values of J_2R^2, suggesting that the two components individually might each have about half of the J_2R^2 predicted in our model.

At a sufficiently large separation, a close binary appears like a large quadrupole in terms of its dynamical effects. For example, Paper II found that a close-in satellite would have

$$J_2R^2 = \frac{1}{2}\frac{q}{(1+q)^2}a_s^2, \tag{3}$$

$$C_{22}R^2 = \frac{1}{4}\frac{q}{(1+q)^2}a_s^2, \tag{4}$$

where $q = m_{Aa}/m_{Ab}$, m_{Aa} and m_{Ab} are the masses of the two (unresolved) components, and a_s is the semimajor axis of the secondary's orbit around the barycenter. For an equal-mass binary composed of two equal-size spheres, $J_2R^2 = \frac{1}{2}a_A^2$, where a_A is the separation between the two components (twice the barycentric a_s).

As discussed below, the inferred value of J_2R^2 for the components of Altjira suggests such an elongated shape that a close inner binary is a reasonable hypothesis. We thus also consider a (close) hierarchical triple model composed of three point masses, also provided by `SPINNY`. Again, to reduce model complexity and avoid degeneracies, our model assumes that only the primary is composed of an unresolved close binary (of two point masses). This "inner" binary is orbited, as before, by the observed second component in the system, which constitutes the "outer" binary.

Many other configurations are possible, such as two "inner" binaries in a hierarchical quadruple system or that the secondary is a close binary orbited by a triaxial primary. The differences between these models cannot be probed by the current observational data, though precise lightcurve observations would help. However, a statistically significant detection of J_2R^2 in our simplified model requires that the two components together deviate from point masses in some way. It also provides measurements of the sum of the angular momentum of the two components and is thus an observational constraint of how the system formed by understanding how angular momentum is partitioned in the system as discussed above.

In principle, `SPINNY` can also model the Sun's gravitational influence on a binary (or triple) system. However, within a critical semimajor axis $a_{\rm crit}$ (given by Equation (3) of P. D. Nicholson et al. 2008), a binary's dynamics are dominated by J_2 rather than the Sun's influence. For the mass and J_2 of Altjira, $a_{\rm crit} \sim 30{,}000$ km. Since Altjira's semimajor axis is well within this boundary, solar gravity can be safely ignored. Thus, for all modeling performed here, we neglect the Sun's influence.

5.1.1. Bayesian Parameter Inference from `MultiMoon`

Given a set of model parameters, `SPINNY` efficiently calculates the relative positions of all the components at all the observation times. `MultiMoon` uses the forward model from `SPINNY` to infer the spin and orbit parameters of our models.[6]

As described in Paper I, `MultiMoon` takes these relative positions and projects them into the plane of the sky as seen from the geocenter (the relative position of the observatories is negligible and ignored), including the light-travel time correction. This provides a model for relative astrometric positions that is then compared to the data assuming independent Gaussian noise with uncertainties listed in Table 2. That is, the χ^2 goodness-of-fit metric for these model parameters is calculated in the usual way. For Altjira, a single χ^2 calculation takes tens of milliseconds for a Keplerian model (which is performed analytically without using `SPINNY`) and about 1 s for the non-Keplerian models.

To explore and understand how the fit is improved by varying parameters, `MultiMoon` uses Bayesian parameter inference powered by *emcee* (D. Foreman-Mackey et al. 2013) as described in Section 2.3 and Paper I. For each `MultiMoon` run, various parameters can be "fixed," or frozen, while other parameters "float." Initial guesses are provided for a large number of "walkers," which allows for multiprocessor calculations that take advantage of our supercomputer resources. After completing a burn-in, the walkers continue to explore the parameter space, where each walker step provides a sample from the posterior probability distribution of the parameters. The ensemble of these samples can then be used to calculate which parameters provide adequate fits to the data. Both the burn-in and total run length are set in advance but confirmed to be appropriate by visual inspection of the chains using plots provided by `MultiMoon`.

Calculation of the Bayesian posterior probabilities requires the choice of priors for all the parameters and a specific noise model that determines the likelihood. The likelihood assumes Gaussian uncertainties; e.g., the log likelihood (to an unimportant constant) is given by $\log\mathcal{L} = -\frac{1}{2}\chi^2$ (e.g., D. W. Hogg et al. 2010). We generally choose uninformative flat priors in all our parameters to allow the observational constraints to control the posterior probabilities. There are two major exceptions. We restrict $C_{22}R^2 \leqslant \frac{1}{2}J_2R^2$ as physically reasonable (see discussion in Paper I and A. C. M. Correia 2018). When modeling a hierarchical triple, we also require the secondary to be less massive than the primary, where this is

[6] MultiMoon is publicly available at https://github.com/dragozzine/multimoon, and the code version we use is essentially the same as used in Paper II, available on Zenodo (doi:10.5281/zenodo.10620251).

now referring to the two (unresolved) components in the "inner" binary. We believe that these prior choices do not significantly affect our conclusions.

5.2. Binary Non-Keplerian Runs

We now turn specifically to our analysis of Altjira. The binary non-Keplerian run refers to our model where the primary is a quadrupole and the secondary is a point mass. Excluding a variety of preliminary and exploratory models (including those discussed in Paper II), our final model of this system used `MultiMoon` with 960 walkers, 20,000 burn-in steps, and 20,000 posterior sampling steps. The resulting 19.2 million posterior samples provide a highly accurate sampling. The `SPINNY` integration tolerance was 10^{-10}, consistent with other analyses and tested to be sufficiently accurate to not introduce significant systematic uncertainties. We fix the spin rate parameter and approximate radius to 1.7453×10^{-4} (rad s^{-1}) and 123 km and confirm that these fixed parameters do not affect the results. (These parameters affect how the orbital motion changes the unobserved spins.)

5.3. Hierarchical Triple Runs

As above, the three-point-mass Altjira fits used 960 walkers, 20,000 burn-in steps, and 20,000 sampling steps. We confirmed that a `SPINNY` tolerance of 10^{-9} did not affect the results.

Three-point-mass models can have 15 free parameters (two sets of six primary-centric orbital elements and three masses), and without astrometric measurements of the inner binary, there are few constraints on its orbit. As a result, our goal was not to provide a full posterior distribution for these fits but rather to find examples of parameter sets that have high posterior probability. This provides a "proof of concept" for three-point-mass models that can adequately match the data. We also note that we fix the eccentricity and argument of periapse of the inner binary to 0 (since any reasonable tidal model would force it to near 0 even with perturbations from the outer component). Although it is not an optimizer (see D. W. Hogg & D. Foreman-Mackey 2018 for discussion), we use `MultiMoon` to explore the parameter space, usually assuming circular orbits. The parameters were initialized by taking the J_2R^2 from the non-Keplerian binary fits and assuming that this was provided by an equal-mass inner binary using Equation (3) for the separation and the orientation angles (e.g., i_{sp} and Ω_{sp}) for the orientation of the inner binary. We note that we did *not* include the center-of-mass–center-of-light offset for the unresolved inner binary, which is a small correction for our analysis but should be considered in future work.

6. Results

Using an exploratory analysis by `MultiMoon` on less data, Paper II found that Altjira showed evidence for non-Keplerian motion. The observed large changes in brightness also require a model that moves beyond point-mass spheres. We confirm statistically significant non-Keplerian motion in our more detailed analysis that includes the three new observations.

First, we consider a Keplerian model. This model reaches a maximum log likelihood of 14.7 corresponding to a minimum χ^2 of 29.4 and a reduced χ^2 of 2.09. Using the χ^2 statistical distribution, there is only a 0.97% chance that the residuals from the Keplerian model are consistent with the assumed noise model. As in Paper II, the orbital parameters for our new Keplerian model were very similar to the previously published parameters in W. M. Grundy et al. (2011) and the orbital parameters in the non-Keplerian fits.

Note that non-Keplerian models explicitly include the Keplerian model as a subset; for example, the binary non-Keplerian model would return $J_2R^2 \approx 0$ if the true model was Keplerian. For this reason, and because a non-Keplerian model is a more accurate representation of the real Altjira system, we prefer to think of the Keplerian model as an extreme version of the non-Keplerian model that has all quadrupole components set to 0 as a prior assumption.

The parameters (giving the 16th, 50th, and 84th percentiles from our posterior samples) for the binary non-Keplerian model of Altjira are reported in Table 3. The posterior distribution for all the parameters is also plotted as a corner plot in Figure 1, which includes one-dimensional marginal distributions for each parameter and two-dimensional joint distributions.

The fit is a significant improvement with a log likelihood of −7.6, with a minimum χ^2 of 15.2 and a reduced χ^2 of 1.68. The probability that a χ^2 value this poor would have occurred assuming an accurate noise model is 8.6%. The best fit is an excellent match to the data as demonstrated by the residuals plot in Figure 2. The improvement in χ^2 from the Keplerian model ($\Delta\chi^2 = 14.2$) is highly statistically significant, even with the addition of six additional parameters. We find a statistically significant J_2R^2 that excludes 0 (the Keplerian case) at $\sim 2.5\sigma$. While this is not overwhelming evidence for non-Keplerian motion, it is clearly preferred over the Keplerian model. Note that the precession period inferred from the best-fit non-Keplerian model is a few thousand years, implying precession of a few degrees. Keplerian fits, including W. M. Grundy et al. (2011), have measured uncertainties of about half a degree for orbital orientation angles, suggesting that even a few degrees of non-Keplerian motion is reasonably detectable.

As expected, $C_{22}R^2$ and ω_{sp} are not meaningfully constrained. In theory, non-Keplerian motion can break the Keplerian degeneracy and measure each mass individually, but our data and model are not sufficient, and the mass estimates for individual components in Table 3 and Figure 1 should not be used. We find that the quadrupole orientation (ϕ) is relatively well aligned (14^{+12}_{-6}°) with the orbit, suggesting that the obliquity of the primary (in the quadrupole model) or the orbit pole of the inner binary (in the hierarchical triple model) is well aligned with the outer binary.

The nominal J_2R^2 of about $17{,}000^{+9000}_{-7000}$ km^2 is quite high for the apparent size of the primary (as estimated from thermal measurements). Even though this value is really like the sum of the oblateness of the two components, it still motivates our investigation of a hierarchical triple three-point-mass model.

As discussed above, we did not perform an exhaustive search of the hierarchical triple parameter space. Our analyses did identify some degeneracies and possibly even multiple solution modes. Even so, we found an example of an excellent fit to the data with such a model, assuming a circular inner binary orbit. This fit has a log likelihood of −5.9 and a χ^2 of 11.8, a substantial improvement to the quadrupole–point-mass model, especially since both have the same number of free parameters. This model has near-equal masses for the inner two components (with a total mass of 3×10^{18} kg) and a (primary-

Table 3
Non-Keplerian Orbit Solution for (148780) Altjira

Parameter	Variable Name	Posterior Distribution	Best Fit	Keplerian Fit
Fitted Parameters				
Primary mass (10^{18} kg)	M_1	$2.7335^{+0.79}_{-0.52}$*	3.547*	⋯
Secondary mass (10^{18} kg)	M_2	$1.3125^{+0.52}_{-0.80}$*	0.5114*	⋯
Semimajor axis (km)	a	9945.56^{+30}_{-30}	9995.99	9944
Eccentricity	e	$0.3511^{+0.0025}_{-0.0024}$	0.3508	0.3523
Inclination (deg)	i	$25.105^{+0.21}_{-0.21}$	25.1134	25.368
Argument of periapse (deg)	ω	$191.69^{+0.45}_{-0.45}$	191.65	192.0
Longitude of the ascending node (deg)	Ω	$274.21^{+0.31}_{-0.31}$	274.26	274.0
Mean anomaly (deg)	$\mathcal{M}$	$124.25^{+0.40}_{-0.41}$	124.28	124.2
Primary zonal gravitational harmonic	J_2R^2	$17,359^{+8759}_{-6906}$	16,219	⋯
Primary sectoral gravitational harmonic	$C_{22}R^2$	3796^{+4203}_{-2691}*	5419*	⋯
Primary rotation axis obliquity (deg)	$i_{\rm sp}$	$19.377^{+5.61}_{-5.34}$	17.614	⋯
Primary rotation axis precession (deg)	$\Omega_{\rm sp}$	243.86^{+19}_{-40}	249	⋯
Primary rotation axis position (deg)	$\omega_{\rm sp}$	181.03^{+123}_{-124}*	191.31*	⋯
Derived parameters				
System mass (10^{18} kg)	$M_{\rm sys}$	$4.0453^{+0.0356}_{-0.0360}$	4.0588	3.99
System density (g cm^{-3})	$\rho_{\rm sys}$	$0.37^{+0.74}_{-0.24}$	0.30	⋯
Primary obliquity with respect to orbit (deg)	ϕ	$14.44^{+12.23}_{-6.20}$	11.810	⋯
Non-Keplerian orbital period (days)	$P_{\rm orb}$	$139.68^{+0.013}_{-0.014}$	139.68	⋯

Note. Orbital and physical parameters from our non-Keplerian binary quadrupole–point-mass fit for Altjira. Parameters marked with an asterisk are not well determined. Full posterior distributions of parameters and degeneracies can be seen in Figure 1. For example, although nominally a non-Keplerian fit can break the mass degeneracy between the two objects, there are not enough data in this case to do so reliably; thus, only the sum of the masses is meaningfully constrained (and unchanged from the Keplerian fit of W. M. Grundy et al. 2011). All fitted angles are relative to the J2000 ecliptic plane on Altjira-centric JD 2454300.0 (2007 July 18, 12:00 UT). For the system density, we use diameters of 246^{+38}_{-139} km and 221^{+31}_{-125} km (E. Vilenius et al. 2014). This fit has a χ^2 of 14.6, and the probability that a χ^2 value this high would be due to random noise is 8.6%, so the fit is statistically acceptable. The non-Keplerian fit is a statistically significant improvement over the Keplerian fit (also shown) based on the improved χ^2. Some hierarchical triple three-point-mass models provide even better fits to the observations, but these were not explored rigorously.

centric) semimajor axis of 124 km (corresponding to an orbital period of about 5.5 hr). We note that this is closer than the sum of the proposed radii, though it is similar to a contact configuration using the 1σ sizes. This is somewhat smaller than expected, as it implies an effective $J_2R^2 \approx 7700\,{\rm km}^2$ from Equation (3). It is possible that a configuration with a semimajor axis around the expected 184 km separation is also consistent with the observations. The inclination and longitude of ascending node of the inner binary for this model are 42° and 190°, respectively, relatively similar to that expected from the binary non-Keplerian fit. Due to the various degeneracies and limited data, we consider the quadrupole–point-mass and the hierarchical triple fit to be reasonably self-consistent and both adequate descriptions of the data with a preference for the hierarchical triple fit since it has a higher likelihood.

We discuss the implications and interpretation of these fits in Section 8 below.

7. The Ongoing Altjira Mutual Event Season

W. M. Grundy et al. (2011) noted that Altjira would have a mutual event season (e.g., shadowings and occultations of the two components) centered around 2028. With our new updated orbit fits, we confirm and update this prediction.

The shapes of the components of Altjira are not known but are clearly not spherical based on our measurement of J_2R^2 as well as significant (∼1 mag) variability in the relative brightness of the components. Including detailed lightcurve observations could provide additional insight to the shapes but only in the presence of multiple assumptions like uniform surfaces, equal albedos, and equal densities. Stellar occultations would provide valuable unique insights, but past predictions for Altjira were generally not well constrained.

It is thus exciting to note that the components of Altjira have just begun their mutual event season! Mutual events can provide detailed information on absolute sizes, shapes, and orientations of the individual objects that then directly constrain albedos and densities. More subtle effects like albedo variegations and phase curves can also be inferred in theory.

However, we provide a cautionary note that mutual events of faint long-period nonspherical TNOs like Altjira can be very complicated to observe and even harder to interpret. The very similar Manwe–Thorondor binary is a valuable example. Mutual event observations were attempted, leading to a complex model with many remaining degeneracies and uncertainties (D. L. Rabinowitz et al. 2020). Multiple nights of highly precise data (requiring $\gtrsim$4 m telescopes) at multiple epochs over several years combined with advanced modeling techniques are likely necessary to get detailed information about Altjira. A more modest goal of measuring approximate sizes and shapes may be more realistic. It does seem plausible that even modest mutual event data could provide constraints on whether the components are themselves contact or close binaries.

A shape model is required for specific details of mutual event predictions like estimated durations, depths, and lightcurve shapes. This is beyond the scope of this paper. However, we can provide the key orbital information needed for future modeling and observing of the Altjira mutual events.

To begin, we provide an ephemeris for the Altjira system from 2023 to 2033 in Table 4. This gives our predicted

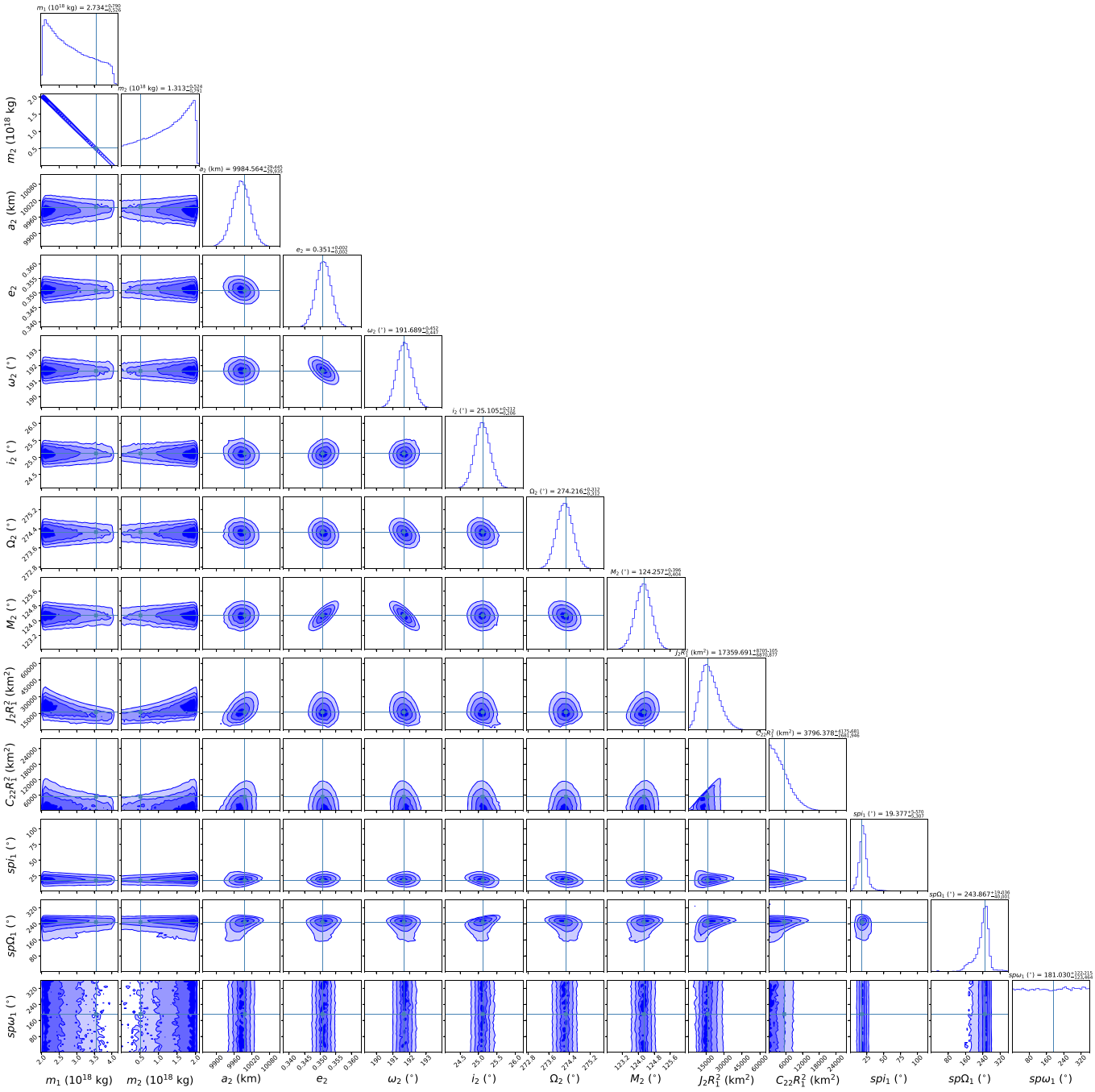

Figure 1. Corner plot for the binary quadrupole–point-mass non-Keplerian Altjira orbit fit. Along the tops of the columns are the marginal posterior distribution for each parameter, which can be used to determine the best fit and uncertainty for Gaussian distributions. The contour plots shows the 1σ, 2σ, and 3σ levels of the joint posterior distributions between every pair of given parameters. Of particular interest is the J_2R^2 posterior, which strongly disfavors the Keplerian model ($J_2R^2 = 0$). Also note that the $C_{22}R^2$ parameter is constrained by the prior $C_{22}R^2 \leqslant J_2R^2/2$ but is not constrained by the data, as expected. All angles are measured relative to the the J2000 ecliptic plane on JD 2454300.0 (2007 July 18, 12:00 UT).

separations and relative positions for the Altjira binary components using our non-Keplerian quadrupole–point-mass model. Uncertainties are calculated using 100 random posterior draws. (We note that this is similar to the methodology used to produce the "Information Gain" calculation discussed in Paper II.) This can be used to make predictions for close approaches, although we note that it collapses the uncertainty in time by expressing the uncertainty only in terms of positions. (More detailed model predictions are available from the authors upon request.)

Using these values, we can determine the properties of close approaches by interpolation. These are presented in Table 5. The x- and y-positions (ΔR.A. cosδ, $\Delta\delta$) and velocities and their uncertainties for each close approach are listed. We also list whether the events are superior (primary in front of secondary) or inferior (secondary in front of primary). We note that a close approach of only 4.3 ± 1.3 mas occurred on 2023 November 3, only a short time after our 2023 October 23 HST observation. Using spheres of the nominal sizes from E. Vilenius et al. (2014), mutual events are expected when

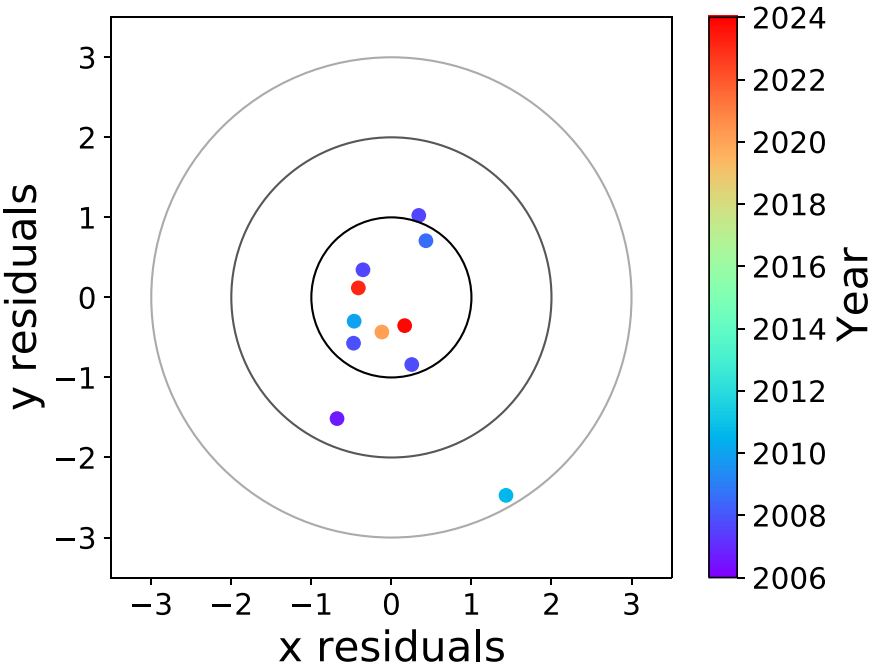

Figure 2. Astrometric residuals for observations shown in Table 2 for the binary quadrupole–point-mass fit. Points are colored as a function of time to illustrate that the residuals show no major time dependence. These residuals are consistent with Gaussian noise (p-value assuming a χ^2 distribution of 8.6%).

Table 4
System Ephemeris

Julian Date	Date	$\Delta\alpha \cos\delta$ (arcsec)	$\Delta\delta$ (arcsec)	$\sigma_{\Delta\alpha \cos\delta}$ (arcsec)	$\sigma_{\Delta\delta}$ (arcsec)	r (arcsec)	σ_r (arcsec)
2459945.500	2023-01-01 00:00:00	−0.31319	0.10624	0.00185	0.00141	0.33073	0.00204
2459945.833	2023-01-01 08:00:00	−0.31180	0.10593	0.00180	0.00139	0.32931	0.00199
2459946.167	2023-01-01 16:00:00	−0.31036	0.10559	0.00175	0.00136	0.32783	0.00194
2459946.500	2023-01-02 00:00:00	−0.30885	0.10524	0.00171	0.00134	0.32629	0.00189
2459946.833	2023-01-02 08:00:00	−0.30729	0.10487	0.00166	0.00132	0.32470	0.00183
2459947.167	2023-01-02 16:00:00	−0.30568	0.10447	0.00162	0.00130	0.32304	0.00178
2459947.500	2023-01-03 00:00:00	−0.30400	0.10406	0.00157	0.00127	0.32132	0.00173
2459947.833	2023-01-03 08:00:00	−0.30227	0.10363	0.00153	0.00125	0.31954	0.00168
2459948.167	2023-01-03 16:00:00	−0.30047	0.10318	0.00148	0.00123	0.31770	0.00163
2459948.500	2023-01-04 00:00:00	−0.29862	0.10271	0.00144	0.00121	0.31579	0.00159

Note. The predicted R.A. and decl. positions of Altjira's secondary from 2023 through 2033. Predicted positions, separations, and uncertainties are taken from a sample of 100 random posterior draws of the binary quadrupole–point-mass model. We display the first 10 rows of the table.

(This table is available in its entirety in machine-readable form in the online article.)

close approaches are less than 7 mas. Since an actual mutual event was likely, our ephemeris implies that the mutual event season for Altjira has already started.

We calculated the close approach predictions using our Keplerian model and our non-Keplerian model to demonstrate that non-Keplerian effects are necessary for accurate mutual event predictions. For example, the separations predicted for the same event differed by ∼3 mas for superior events and ∼5 mas for inferior events, comparable to the sizes of the components. The mutual event season is about 1.5 yr earlier in the non-Keplerian model and centered roughly on 2026, which partially explains why our predicted mutual events have started so soon. Timing predictions differed by about 0.5 hr, growing to 1.5 hr for superior events, comparable to the estimated timing uncertainties. However, for inferior events, the timing predictions were different between Keplerian and non-Keplerian by 32–50 hr! Inferior events happen near apoapse, so the precession included in non-Keplerian modeling has a larger lever arm; furthermore, the velocity is slower so that a larger distance in position corresponded to an even larger difference in timing. We conclude that including non-Keplerian effects can make a significant difference in mutual event predictions.

Given the sensitivity of the predictions to small effects, it is also worth mentioning that unmodeled systematic uncertainties could lead to significant offsets from our predicted close approaches. Possible systematic uncertainties are not included in Table 5.

Shadowing events are not shown in Table 5. Calculation of the shadowing events (based on predictions for close approaches as seen from the perspective of the Sun) shows that they are about ±1 mas separated from the occultations and occur at a similar time for superior events and about 2 hr earlier for inferior events. Differences in Keplerian and non-Keplerian predictions for shadowing are very similar to the differences seen in occultations.

Table 5
Close Approaches for (148780) Altjira

Julian Date	Date	Sep. (mas)	Sep. Err. (mas)	x (mas)	x Err. (mas)	y (mas)	y Err. (mas)	x Vel. (mas hr^{-1})	y Vel. (mas hr^{-1})	Event Type
2459972.49306	2023-01-27 23:50:00	8.327	1.262	2.714	0.851	7.872	0.932	0.743	−0.256	Sup.
2460112.43403	2023-06-16 22:25:00	6.287	1.253	2.103	0.850	5.925	0.921	0.713	−0.253	Sup.
2460165.81944	2023-08-09 07:40:00	8.602	6.980	−2.823	6.192	−8.126	3.223	−0.386	0.135	Inf.
2460252.23611	2023-11-03 17:40:00	4.272	1.339	1.449	0.912	4.019	0.981	0.747	−0.266	Sup.
2460304.80208	2023-12-26 07:15:00	10.374	7.322	−3.328	6.490	−9.826	3.390	−0.409	0.139	Inf.
2460391.64236	2024-03-22 03:25:00	6.708	1.334	2.298	0.904	6.302	0.980	0.724	−0.261	Sup.
2460444.63542	2024-05-14 03:15:00	10.381	7.221	−3.475	6.390	−9.782	3.364	−0.381	0.135	Inf.
2460531.75347	2024-08-09 06:05:00	2.781	1.370	0.956	0.941	2.612	0.996	0.721	−0.265	Sup.
2460585.47569	2024-10-01 23:25:00	3.871	7.713	−1.307	6.805	−3.643	3.632	−0.393	0.143	Inf.
2460671.22222	2024-12-26 17:20:00	3.699	1.443	1.295	0.987	3.465	1.053	0.746	−0.274	Sup.
2460723.95486	2025-02-17 10:55:00	8.925	7.773	−2.997	6.855	−8.406	3.663	−0.397	0.142	Inf.
2460810.94097	2025-05-15 10:35:00	3.774	1.419	1.327	0.973	3.532	1.032	0.710	−0.267	Sup.
2460864.88889	2025-07-08 09:20:00	3.666	7.869	−1.302	6.919	−3.427	3.748	−0.375	0.142	Inf.
2460950.93750	2025-10-02 10:30:00	0.193	1.505	0.077	1.045	0.177	1.083	0.735	−0.278	Sup.
2461004.59375	2025-11-25 02:15:00	1.669	8.377	−0.573	7.353	−1.568	4.014	−0.400	0.149	Inf.
2461090.26736	2026-02-18 18:25:00	2.939	1.527	1.069	1.051	2.738	1.107	0.731	−0.278	Sup.
2461143.67014	2026-04-13 04:05:00	5.150	8.227	−1.832	7.214	−4.813	3.955	−0.380	0.145	Inf.
2461230.29167	2026-07-08 19:00:00	0.170	1.533	0.052	1.069	0.162	1.098	0.710	−0.276	Sup.
2461284.88542	2026-09-01 09:15:00	2.570	8.624	0.944	7.537	2.390	4.191	−0.378	0.150	Inf.
2461369.96875	2026-11-25 11:15:00	1.022	1.634	−0.384	1.142	−0.948	1.168	0.743	−0.289	Sup.
2461423.55556	2027-01-18 01:20:00	0.817	8.894	−0.294	7.767	−0.762	4.333	−0.396	0.153	Inf.
2461509.46875	2027-04-13 23:15:00	0.939	1.609	0.320	1.121	0.883	1.154	0.713	−0.282	Sup.
2461563.84722	2027-06-07 08:20:00	0.961	8.798	0.354	7.666	0.893	4.318	−0.368	0.149	Inf.
2461649.56944	2027-09-01 01:40:00	3.150	1.675	−1.165	1.186	−2.927	1.182	0.720	−0.289	Sup.
2461704.32639	2027-10-25 19:50:00	6.594	9.385	2.484	8.157	6.108	4.642	−0.387	0.157	Inf.
2461788.95833	2028-01-18 11:00:00	1.462	1.738	−0.532	1.222	−1.361	1.236	0.737	−0.296	Sup.
2461842.89583	2028-03-12 09:30:00	1.230	9.320	0.448	8.094	1.146	4.621	−0.381	0.155	Inf.
2461928.79861	2028-06-06 07:10:00	2.255	1.714	−0.845	1.214	−2.090	1.210	0.703	−0.289	Sup.
2461984.05903	2028-07-31 13:25:00	7.929	9.520	3.123	8.242	7.288	4.764	−0.366	0.156	Inf.
2462068.69097	2028-10-24 04:35:00	5.327	1.825	−2.060	1.305	−4.913	1.275	0.733	−0.302	Sup.
2462123.31944	2028-12-17 19:40:00	8.083	10.018	3.108	8.660	7.461	5.035	−0.390	0.162	Inf.
2462208.05208	2029-03-12 13:15:00	2.484	1.823	−0.954	1.293	−2.294	1.285	0.719	−0.299	Sup.
2462262.81597	2029-05-06 07:35:00	5.915	9.801	2.330	8.459	5.436	4.950	−0.365	0.157	Inf.
2462348.13194	2029-07-30 15:10:00	5.862	1.851	−2.283	1.333	−5.399	1.284	0.707	−0.299	Sup.
2462487.69097	2029-12-17 04:35:00	6.153	1.956	−2.404	1.406	−5.664	1.359	0.737	−0.312	Sup.
2462542.36111	2030-02-09 20:40:00	8.972	10.482	3.569	9.011	8.231	5.353	−0.381	0.165	Inf.
2462627.30556	2030-05-05 19:20:00	4.850	1.916	−1.929	1.377	−4.450	1.332	0.703	−0.303	Sup.
2462767.35764	2030-09-22 20:35:00	8.907	2.012	−3.532	1.468	−8.177	1.376	0.719	−0.313	Sup.
2462906.70139	2031-02-09 04:50:00	6.577	2.055	−2.633	1.485	−6.027	1.419	0.725	−0.316	Sup.
2463046.64583	2031-06-29 03:30:00	8.236	2.039	−3.359	1.490	−7.519	1.392	0.697	−0.310	Sup.
2463186.42708	2031-11-15 22:15:00	10.624	2.169	−4.292	1.594	−9.718	1.471	0.730	−0.325	Sup.
2463325.85069	2032-04-03 08:25:00	7.932	2.140	−3.276	1.562	−7.224	1.463	0.706	−0.318	Sup.
2463465.95139	2032-08-21 10:50:00	11.765	2.197	−4.866	1.628	−10.712	1.474	0.704	−0.322	Sup.
2463605.40972	2033-01-07 21:50:00	11.135	2.293	−4.626	1.691	−10.129	1.549	0.728	−0.333	Sup.
2463745.14583	2033-05-27 15:30:00	10.635	2.245	−4.486	1.661	−9.643	1.510	0.693	−0.322	Sup.
2463885.11806	2033-10-14 14:50:00	14.455	2.370	−6.134	1.773	−13.089	1.573	0.717	−0.335	Sup.

Note. Close approaches are defined as events where the primary and secondary are separated by less than 15 mas, not necessarily implying a mutual event. x and y correspond to $\Delta\alpha \cos\delta$ and $\Delta\delta$, respectively. Note that timing and depth uncertainty are significant for inferior events.

We can provide some context about the expected depth and duration of mutual events assuming different shape models. First, we note that since the two components have similar brightness, a perfect shadowing and/or occultation would lead to a ∼50% drop in flux for an object that is typically $V \simeq 23$ mag in brightness. Nonzero impact parameters and nonspherical shapes suggest that this would be rare; ∼10% drops in flux should be common for the closest approaches. Since the objects are probably similar in size, these drops should generally be gradual; e.g., ingress and egress times are about half of the event durations. The fastest expected brightness changes are ∼0.1 mag hr^{-1}.

To estimate durations, we begin by noting that Altjira's typical distance is 45 au, where 1 mas corresponds to about 32 km. Taking the sizes from E. Vilenius et al. (2014), this gives radii of approximately $3.8^{+0.6}_{-2.2}$ and $3.4^{+0.5}_{-2.0}$ mas, but this assumes low equal albedos, equal densities, and spherical shapes. Perhaps this is representative of the long axis of a nonspherical shape. If we assume spherical shapes and -1σ radii of 1.6 and 1.4 mas, then a grazing event requires a close approach distance of only 3.0 mas. About 10 such events are predicted, most of which have uncertainties that are reasonably small so that the statistical expectation is a ∼95% chance of

some kind of event (especially when including shadowing). There is significant correlation in the predicted close approach distances so that clear observation and interpretation of an earlier event could shrink uncertainties in later events. New additional astrometric measurements may help somewhat, especially later in the mutual event season. Conversely, precise mutual events with clear interpretations can provide effective astrometric observations.

Continuing with the small sphere model (1.6 and 1.4 mas radii) and using the velocities given in Table 5, a central superior event would last about 3.5 hr, and a central inferior event would last about 7 hr. Noncentral events are correspondingly shorter, though multiple events would have $\gtrsim$1 hr expected durations. If the objects are bigger (in some direction), then these durations grow correspondingly.

All things considered, about ~10 close approaches are likely to yield strong mutual events. Several other close approaches could lead to detectable mutual events if the components are larger than expected, nonspherical, or composed of close binaries, as we have hypothesized.

If one or both of the components is a close binary, this changes the mutual event predictions because the components are smaller (e.g., 1.1 mas if equal-mass, equal-albedo, equal-density spheres) and because this inner binary would have orbital motion that could be a few times faster than the outer binary motion. This is similar to how an elongated object rotating on a similar timescale to the mutual event duration can significantly affect the shape of the resulting lightcurve. However, the inner binary separation would also allow for mutual events at larger separations.

Furthermore, because the inner binary is so close together, mutual events between inner binary components would be much more likely. If the inner and outer binaries are even reasonably closely aligned, similar to what is seen in our fits, inner mutual events could also be happening now on a ~nightly basis. Depending on the separation and orientation of the inner binary components, lightcurve observations could potentially distinguish between a close binary, a contact binary, and a single triaxial ellipsoid.

We suggest that the next step in preparing for Altjira's mutual events would be a detailed lightcurve of the system. Such a lightcurve could detect inner mutual events or at least provide information on the amplitudes, periods, and shapes of the two components. This information is a prerequisite to precise mutual event model prediction and interpretation. We note that the binary components are sometimes separated by 0.″3, which could lead to resolved lightcurves with high-quality ground-based data under great seeing with PSF modeling. The ephemeris in Table 4 can be used to predict such ideal observational times.

As a final word of caution, we note that our ephemeris and predictions depend on our model assumptions. It is possible that a similar difference between the Keplerian and non-Keplerian models would also be found in different non-Keplerian models (such as a two-quadrupole model). Given the statistical and systematic uncertainties, observing for as long as possible before and after the nominal events is prudent.

We also speculate that inaccurate orbital modeling may be a major contributing factor to the fact that mutual events have not yet fulfilled their promise of improved characterization of other TNO binaries (e.g., D. Ragozzine & M. E. Brown 2009; D. L. Rabinowitz et al. 2020). For example, the error in the ephemeris for Haumea identified in B. C. N. Proudfoot et al. (2024a) could have contributed to the challenges of interpreting observed mutual events, though Hi'iaka's unexpectedly strong lightcurve also contributed (D. M. Hastings et al. 2016).

8. Discussion

Given the observed non-Keplerian motion in Altjira, what can we say about its shape? As noted above, $J_2R^2 = 17{,}000^{+9000}_{-7000}$ km^2 is not precisely detected and is unrealistically assumed to be entirely attributable to the primary (with a point-mass secondary). Still, to guide future interpretation, we can comment on the implications of these measurements for the shape of Altjira's primary.

To convert a measurement of J_2R^2 to a particular three-dimensional mass configuration requires assuming a shape model as well as a nominal size and a value of $C_{22}R^2$. For example, we computed triaxial ellipsoid models using Equations (1) and (2) using a polar radius $c = 123$ km (the nominal radius from thermal measurements), and $C_{22}R^2 = 4000$ km^2 implies semiaxes of 374 × 243 × 123 km and a density of only 0.06 g cm^{-3}. Using the maximal $C_{22}R^2$ of $J_2R^2/2$ (which sets the intermediate axis to be equal to the polar axis) gives a shape of 430 × 123 × 123 km and a density of 0.11 g cm^{-3}. With the same values for the gravitational harmonics, a polar radius of c = 73.5 (the -1σ radius from thermal measurements) results in semiaxes of 418 × 73.5 × 73.5 km and a density of 0.32 g cm^{-3}.

The most extreme known solar system objects typically have axis ratios of less than 2.5. For example, the extreme shape of Trojan asteroid Polymele is inferred to be 13 × 12 × 5 km (H. Levison 2024, personal communication). While we did not test every variation of the parameters, there seems to be no set of parameters where the shape was less extreme than Polymele and the density higher than the lowest TNO density measurements of ~0.2 g cm^{-3}. This can be alleviated by using a smaller than nominal J_2R^2 either due to uncertainties or by noting that the nominal J_2R^2 assumes that all of the J_2R^2 is concentrated in the primary. Overall, a triaxial ellipsoid is typically an unsatisfactory shape model.

We consider a Cassinoid as a flexible model that approximates a contact binary while being similar to observed small bodies. A Cassinoid has a dumbbell-like shape, closely representing the dumbbell figures of a rotating, self-gravitating fluid body. (We note that a Roche model assumes fluid strength-less interiors which are not an ideal physical characterization of small TNO components.) It is very useful as it has a simple algebraic representation that can easily be used to calculate moments of inertia analytically. See the Appendix of P. Descamps (2015) for more information about Cassinoids. For the nominal J_2R^2 and mass of Altjira, we find that the minimum size of a Cassinoid model would require a density of 0.2 g cm^{-3}, a rather low value and also somewhat inconsistent with the thermal size measurements. Considering uncertainties suggests that a Cassinoid model has a ~20% chance of being an acceptable description of the observations.

To reach the higher nominal J_2R^2 values implied by our fits requires rejecting the contact binary model and adopting components that are physically separated. For example, two spheres with density of 0.5 g cm^{-3} (1 g cm^{-3}) could be explained by components of ~85 km (~70 km) in radius, separated by 300–450 km. This would also be more consistent with the thermal models, assuming that these measure the total

surface area. We note again that a similar close hierarchical triple configuration was found to be an excellent fit to the observations.

Such a triple would not be resolvable by any current telescope. It would also be more robust to possible issues of dynamical stability than Lempo (Paper I) since it would be much more hierarchical than Lempo ($a_{out}/a_{in} \simeq 40$ instead of 5.5 for Lempo).

More advanced modeling of the shape of the components of Altjira would be justified once lightcurve modeling (and then mutual events) can provide additional constraints on relative sizes and shapes. We also encourage the community to explore opportunities to measure stellar occultations of the Altjira components. Finally, we note that Altjira is scheduled to be observed by JWST, which should provide some additional insight into this system.

This nominal configuration is relatively similar to Lempo, although the ratio of the outer and inner binary separations is larger. Without knowledge of how the mass is distributed between the inner and outer binary—which is not well determined in our model—we cannot directly assess how the angular momentum is distributed among the components. However, it appears that, unlike the Lempo system, most of the angular momentum for Altjira is in the outer binary. Whether such a configuration is a reasonable outcome of gravitational collapse triggered by SI requires more advanced collapse models.

Another formation model to consider for cold classical hierarchical triples is formation by binary–binary encounters (e.g., A. Brunini & M. C. López 2020). Such encounters are relatively common for binaries as wide as Altjira and are not adequately studied. Like Lempo, Altjira's inner and outer binaries are relatively well aligned, which is not a common outcome of these encounters, though additional modeling is also needed to better understand this scenario.

9. Conclusions

TNO (148780) Altjira is proposed to be a cold classical TNO binary with an unusually high inclination. Such cold classical binaries are thought to be formed through gravitational collapse after the SI. Altjira's configuration is consistent with these models and provides motivation for improved models that can resolve the angular momentum contribution of individual TNO binary components. It is also possible that Altjira formed or was modified by binary–binary encounters.

We have modeled the non-Keplerian orbit of Altjira, adding the newest HST data from 2023, which we analyzed using the new PSF fitting routine `nPSF`, as presented in this paper. Using the astrometry output from `nPSF` and astrometry from past HST visits and Keck data between 2006 and 2020, we modeled Altjira in different configurations with our Bayesian parameter inference tool `Multimoon` (Paper I).

We confirmed that a non-Keplerian model for Altjira was preferred over a Keplerian model at the $\sim 2.5\sigma$ level. A binary quadrupole–point-mass model finds an oblateness of $J_2R^2 = 17{,}000^{+9000}_{-7000}\,\mathrm{km}^2$, which is large than expected for the size of Altjira. Even considering that the non-Keplerian effects are likely due to both shapes, neither a triaxial ellipsoid nor a Cassinoid (dumbbell) model are satisfactory for the majority of our uncertainty region. We thus propose that one or both of the components of Altjira are near-equal-mass unresolved "inner" binaries. This is consistent with our result that a hierarchical triple configuration is the best match for the data, though we did not explore this parameter space in detail. We thus conclude that Altjira is likely an unresolved hierarchical triple.

We also call attention to Altjira's ongoing mutual event season. After obtaining detailed lightcurves, mutual event observations could provide significantly improved understanding of the shapes, sizes, albedos, and densities of the components of this system. We provide an ephemeris for close approaches in this system—which is different from the prediction using Keplerian orbits—but leave detailed predictions for future work. We note that mutual event interpretations are challenging, as seen for the very similar Manwe–Thorondor system (D. L. Rabinowitz et al. 2020).

A self-consistent analysis of the physical properties of the components of Altjira that combines mass and J_2R^2 measurements, thermal constraints, lightcurve shapes, and eventually mutual event data would be able to determine detailed information about the sizes, shapes, and configurations of this primordial likely triple TNO.

Acknowledgments

We acknowledge the support of Dallin Spencer with various aspects of `MultiMoon` fitting and general help. We acknowledge many cohorts of Brigham Young University Physics 529 students who worked on or tested various versions of `nPSF`, including Kyle Adams, Crystal-Lynn Bartier, Scott Call, Ian Clark, Jared Davidson, Jarrod Hansen, Jacob Jensen, Daniel Jones, Emma Rasmussen, Rochelle Steele, Savanah Turner, Nicholas Wallace, and Denzil Watts. We also thank the BYU Office of Research Computing for their dedication to providing computing resources, without which this work would not have been possible.

This research is based on observations made with the NASA/ESA HST obtained from the Space Telescope Science Institute, which is operated by the Association of Universities for Research in Astronomy, Inc., under NASA contract NAS 5-26555. These observations are associated with program 17206. Support for this work was funded by grants associated with this program. Some of the data presented in this article were obtained from the Mikulski Archive for Space Telescopes (MAST) at the Space Telescope Science Institute. The specific observations analyzed can be accessed via MAST doi:10.17909/ht9x-nt22.

Some of the data presented herein were obtained at Keck Observatory, which is a private 501(c)3 nonprofit organization operated as a scientific partnership among the California Institute of Technology, the University of California, and the National Aeronautics and Space Administration. The Observatory was made possible by the generous financial support of the W. M. Keck Foundation.

The authors wish to recognize and acknowledge the very significant cultural role and reverence that the summit of Maunakea has always had within the Native Hawaiian community. We are most fortunate to have the opportunity to conduct observations from this mountain.

ORCID iDs

Maia A Nelsen https://orcid.org/0000-0001-8780-8480
Darin Ragozzine https://orcid.org/0000-0003-1080-9770
Benjamin C. N. Proudfoot https://orcid.org/0000-0002-1788-870X
William G. Giforos https://orcid.org/0000-0001-6838-1530
Will Grundy https://orcid.org/0000-0002-8296-6540

References

Benecchi, S. D., Noll, K. S., Grundy, W. M., & Levison, H. F. 2010, Icar, 207, 978
Brunini, A., & López, M. C. 2020, MNRAS, 499, 4206
Campbell, H. M., Stone, L. R., & Kaib, N. A. 2023, AJ, 165, 19
Correia, A. C. M. 2018, Icar, 305, 250
Descamps, P. 2015, Icar, 245, 64
Foreman-Mackey, D., Hogg, D. W., Lang, D., & Goodman, J. 2013, PASP, 125, 306
Gelman, A., Vehtari, A., Simpson, D., et al. 2020, arXiv:2011.01808
Grundy, W. M., Benecchi, S. D., Rabinowitz, D. L., et al. 2012, Icar, 220, 74
Grundy, W. M., Noll, K. S., Nimmo, F., et al. 2011, Icar, 213, 678
Grundy, W. M., Noll, K. S., Roe, H. G., et al. 2019, Icar, 334, 62
Grundy, W. M., Noll, K. S., Virtanen, J., et al. 2008, Icar, 197, 260
Hastings, D. M., Ragozzine, D., Fabrycky, D. C., et al. 2016, AJ, 152, 195
Hogg, D. W., Bovy, J., & Lang, D. 2010, arXiv:1008.4686
Hogg, D. W., & Foreman-Mackey, D. 2018, ApJS, 236, 11
Huang, Y., Gladman, B., & Volk, K. 2022, ApJS, 259, 54
Krist, J. E., Hook, R. N., & Stoehr, F. 2011, Proc. SPIE, 8127, 81270J
Le Mignant, D., van Dam, M. A., Bouchez, A. H., et al. 2006, Proc. SPIE, 6272, 627201
Leiva, R., Buie, M. W., Keller, J. M., et al. 2020, PSJ, 1, 48
Malhotra, R., & Roy, S. 2023, RNAAS, 7, 143
Matheson, I. C., Malhotra, R., & Keane, J. T. 2023, MNRAS, 522, 3298
McCully, C., & Tewes, M., 2019 Astro-SCRAPPY: Speedy Cosmic Ray Annihilation Package in Python, Astrophysics Source Code Library, ascl:1907.032
McKinnon, W. B., Richardson, D. C., Marohnic, J. C., et al. 2020, Sci, 367, aay6620
Nesvorný, D., Li, R., Simon, J. B., et al. 2021, PSJ, 2, 27
Nesvorný, D., Li, R., Youdin, A. N., Simon, J. B., & Grundy, W. M. 2019, NatAs, 3, 808
Nesvorný, D., & Vokrouhlický, D. 2019, Icar, 331, 49
Nesvorný, D., Youdin, A. N., & Richardson, D. C. 2010, AJ, 140, 785
Nicholson, P. D., Cuk, M., Sheppard, S. S., Nesvorny, D., & Johnson, T. V. 2008, The Solar System Beyond Neptune (Tucson, AZ: Univ. Arizona Press), 411
Polak, B., & Klahr, H. 2023, ApJ, 943, 125
Proudfoot, B. C. N., Ragozzine, D. A., Giforos, W., et al. 2024a, PSJ, 5, 69
Proudfoot, B. C. N., Ragozzine, D. A., Thatcher, M. L., et al. 2024b, AJ, 167, 144
Rabinowitz, D. L., Benecchi, S. D., Grundy, W. M., Verbiscer, A. J., & Thirouin, A. 2020, AJ, 159, 27
Ragozzine, D., & Brown, M. E. 2009, AJ, 137, 4766
Ragozzine, D., Pincock, S., Proudfoot, B. C. N., et al. 2024, arXiv:2403.12785
Robinson, J. E., Fraser, W. C., Fitzsimmons, A., & Lacerda, P. 2020, A&A, 643, A55
Sheppard, S. S. 2007, AJ, 134, 787
Showalter, M. R., Benecchi, S. D., Buie, M. W., et al. 2021, Icar, 356, 114098
The Astropy Collaboration, Robitaille, T. P., Tollerud, E. J., et al. 2013, A&A, 558, A33
van de Schoot, R., Depaoli, S., King, R., et al. 2021, Nat. Rev. Methods Primers, 1, 1
van Dokkum, P. G. 2001, PASP, 113, 1420
Vilenius, E., Kiss, C., Müller, T., et al. 2014, A&A, 564, A35
Yelda, S., Lu, J. R., Ghez, A. M., et al. 2010, ApJ, 725, 331